ARTICLE

Miniaturized Implantable Fluorescence Probes Integrated with Metal−Organic Frameworks for Deep Brain Dopamine Sensing

Wei Ling, Xue Shang, Chaonan Yu, Chenxi Li, Kedi Xu, Linqing Feng, Yina Wei, Tao Tang,* and Xian Huang*

Cite This: https://doi.org/10.1021/acsnano.4c00632
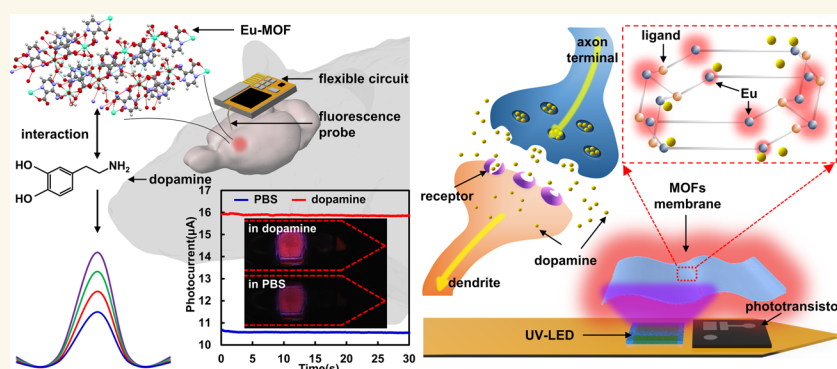
Read Online

ACCESS | 📊 Metrics & More | 📄 Article Recommendations | 🆂🅸 Supporting Information

ABSTRACT: Continuously monitoring neurotransmitter dynamics can offer profound insights into neural mechanisms and the etiology of neurological diseases. Here, we present a miniaturized implantable fluorescence probe integrated with metal−organic frameworks (MOFs) for deep brain dopamine sensing. The probe is assembled from physically thinned light-emitting diodes (LEDs) and phototransistors, along with functional surface coatings, resulting in a total thickness of 120 μm. A fluorescent MOF that specifically binds dopamine is introduced, enabling a highly sensitive dopamine measurement with a detection limit of 79.9 nM. A compact wireless circuit weighing only 0.85 g is also developed and interfaced with the probe, which was later applied to continuously monitor real-time dopamine levels during deep brain stimulation in rats, providing critical information on neurotransmitter dynamics. Cytotoxicity tests and immunofluorescence analysis further suggest a favorable biocompatibility of the probe for implantable applications. This work presents fundamental principles and techniques for integrating fluorescent MOFs and flexible electronics for brain-computer interfaces and may provide more customized platforms for applications in neuroscience, disease tracing, and smart diagnostics.

KEYWORDS: implantable flexible electronics, metal−organic framework, fluorescence probe, dopamine sensor, brain-computer interface

Continuously tracking neurotransmitter dynamics holds tremendous potential for revealing the intricacies of the brain, as neurotransmitters orchestrate a myriad of complex biological processes that underpin human cognition, behavior, and perception.[1] While traditional techniques like microdialysis,[2] positron emission tomography,[3] and Raman spectroscopy[4] have contributed valuable insights into neurotransmitter dynamics, they often suffer from bulky equipment and discrete sensing modes. Advancements in *in vivo* neurotransmitter sensing have resulted in various miniaturized devices, including silicon-based electrochemical probes,[5,6] needle-type field-effect transistors,[7,8] and tapered optical

fibers.[9,10] Despite favorable sensing performance, these rigid devices are mechanically incompatible with soft biological tissues, potentially leading to tissue infection, signal fluctuations, and even performance failures. This misalignment with
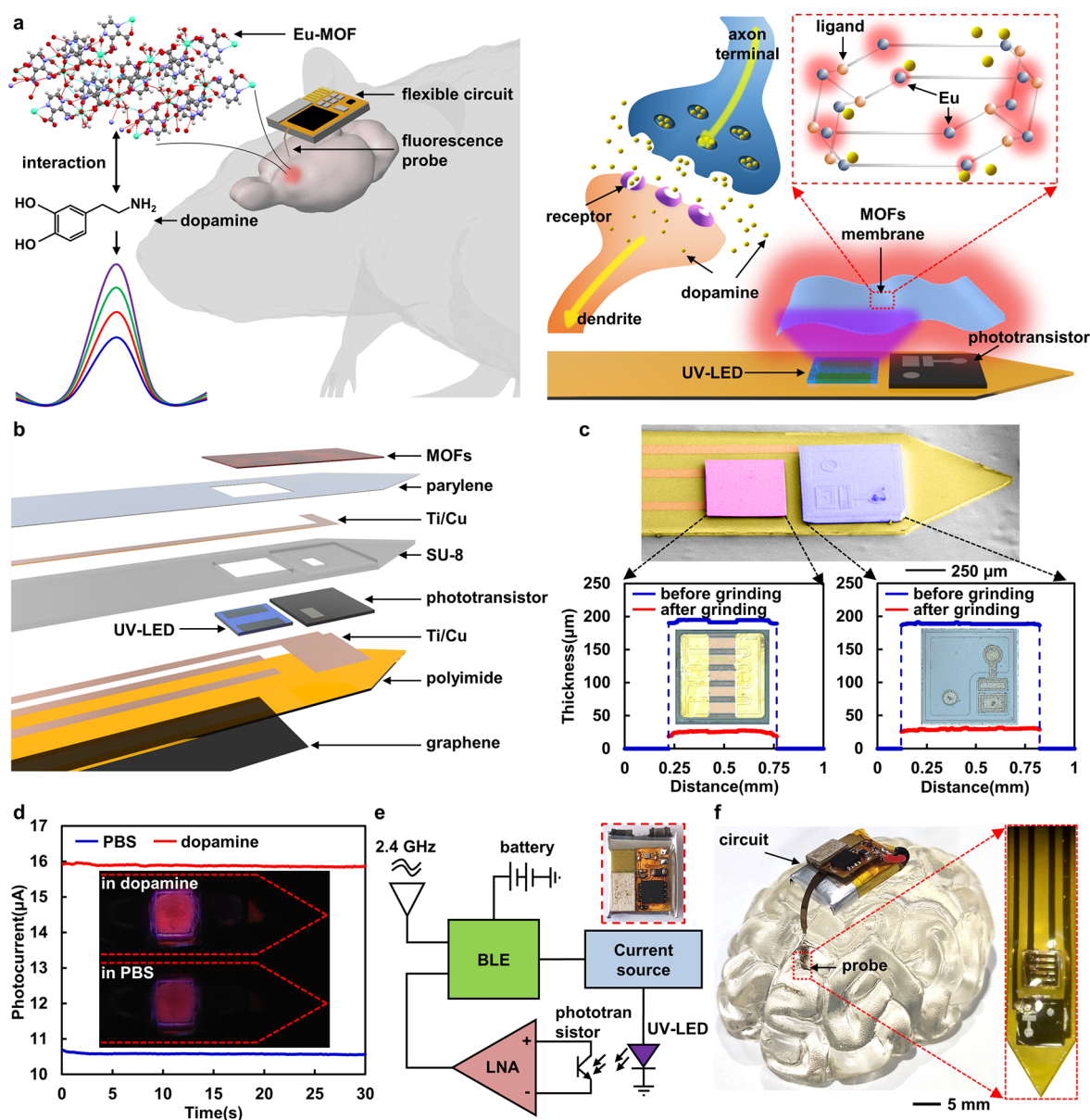
Figure 1. Overview of the implantable fluorescence probe for deep brain dopamine sensing. (a) Schematics showing the conformal integration of an implantable probe into soft brain tissue and the corresponding working mechanism of dopamine sensing. A fluorescent MOF film that specifically binds dopamine was modified onto the probe, which simultaneously excited the fluorescence and detected the fluorescence intensity. (b) The multilayer structure of the probe containing a UV-LED as a light source and a phototransistor for fluorescence detection. (c) A SEM image showing the surface topography of the probe. Bottom: corresponding topography measurements of the UV-LED and phototransistor before and after grinding. (d) Photocurrent response of the fluorescence probe in PBS and high-concentration dopamine solution, respectively. Inset: images showing the fluorescence intensity of the probe. (e) Schematic showing the composition of the wireless circuit. Inset: an image of the wireless flexible circuit. (f) An image showing a brain phantom implanted with a flexible fluorescence probe. Inset: an enlarged image showing an implantable probe with a needle-like tip.

the requirement for long-term, biocompatible tissue-electronic interfaces underscores the need for further innovation in this field.

Flexible electronics leveraging mechanical flexibility and integratable functionality have transformed modern healthcare with numerous applications in brain-computer interface,[11,12] smart healthcare,[13,14] and point-of-care testing.[15,16] Particularly, the seamless integration of flexible electronics with naturally curved brain tissues has yielded diverse implantable neurotransmitter sensors, such as polymer-field-effect transistors and carbon-based electrodes.[17,18] Nonetheless, most of them rely on electrical or electrochemical principles, which

necessitate a certain period to stabilize, continuously consume the analyte, and are susceptible to interference from background noises and other species.[19,20] Fluorescent sensors have enabled long-lived and specific chemical sensing without depleting the targeted analyte while providing favorable resistance to electromagnetic interference.[21,22] Yet, implantable fluorescent sensors for neurotransmitter sensing have rarely been reported due to the limited availability of suitable fluorescent materials and miniaturized photometers. Microscale light-emitting diodes (μ-LEDs) with small size and high luminous efficiency have been successfully applied for sensing and stimulating internal organs,[23,24] holding the potential to
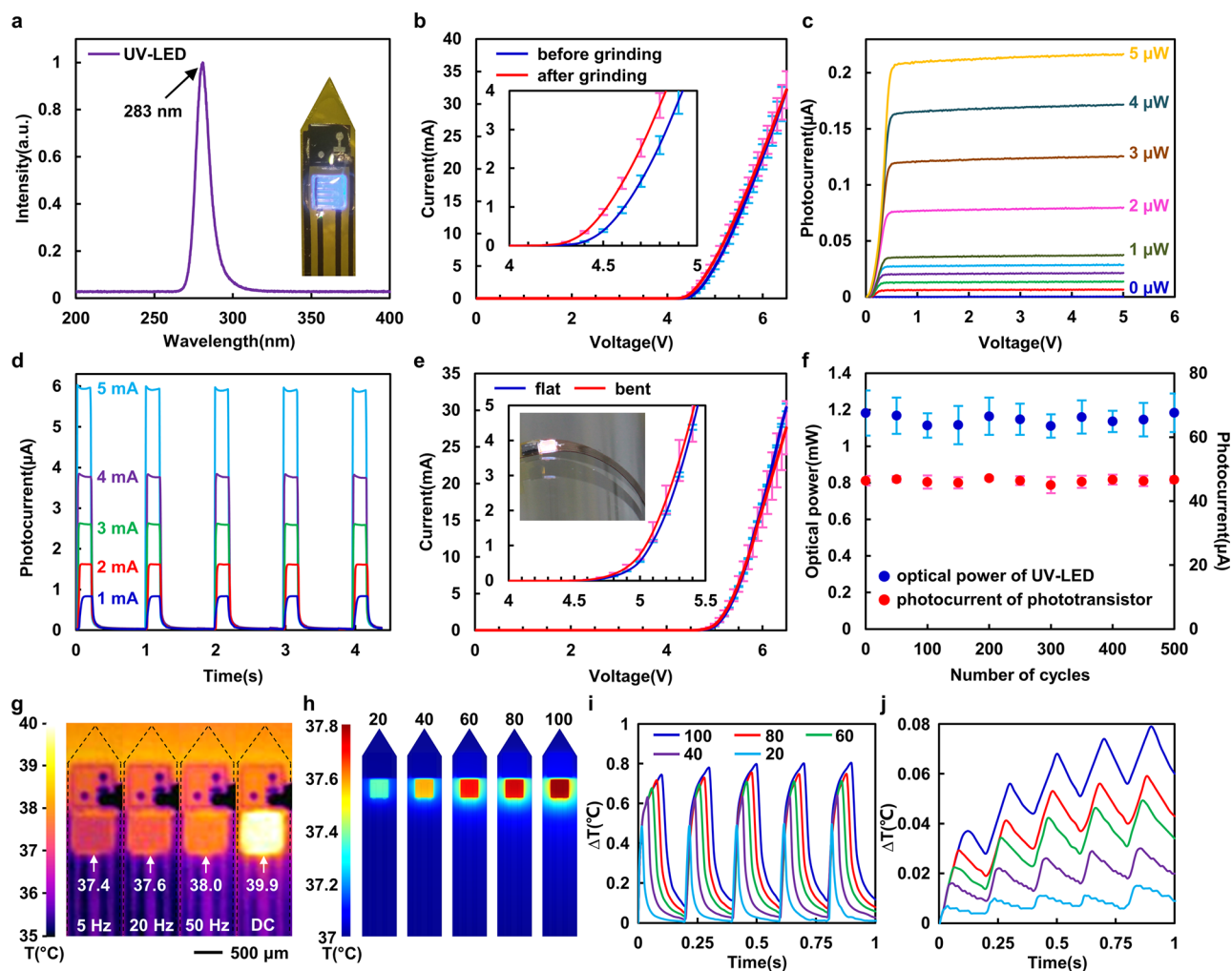
Figure 2. Optoelectronic, mechanical, and thermal properties of the probe. (a) Electroluminescent spectrum of the UV-LED embedded in the probe. Inset: a probe with a UV-LED turned on. (b) Current−voltage characteristics of UV-LEDs before and after grinding. Inset: enlarged curves at low current, ranging from 0 to 4 mA. $n = 3$, error bars indicate mean ± SD. (c) Collector characteristic curves of the ground phototransistor under simulated solar illumination with optical power levels ranging from 0 to 5 μW. (d) Photocurrents of the phototransistor at different fluorescence intensities activated by the embedded UV-LED. (e) Current−voltage characteristics of the probes in flat and bent states. Insets: enlarged curves at low current, ranging from 0 to 5 mA, and a probe attached to a cylinder with a curvature radius of 5 mm. $n = 3$, error bars indicate mean ± SD. (f) Optical power of UV-LEDs at 1 mA current and photocurrent of phototransistors under 1 mW solar illumination during 500 cycles of bending. $n = 3$, error bars indicate mean ± SD. (g) Temperature profiles of the probe when the UV-LED operated at different frequencies with a constant current of 1 mA. (h) Thermal modeling of the probe operating at a current of 1 mA, a frequency of 5 Hz, and different pulse widths from 20 to 100 ms. Temperature variation of the (i) UV-LED and (j) phototransistor as a function of different pulse widths.

develop injectable photometers for deep brain fluorescence sensing. Additionally, one promising class of material candidates for implantable fluorescent sensors are metal−organic frameworks (MOFs), which are highly ordered crystals known for their tunable structure, high surface area, and versatility.[25] Despite some demonstrations of MOFs-based chemical sensors,[26−29] they have not been implemented in fluorescent devices for neurochemical sensing. Their untapped but attractive potential for implantable biomedical applications requires intensive investigation.

Here, we present a miniaturized implantable probe integrated with fluorescent MOFs for deep brain dopamine sensing. The probe consists of a microscale ultraviolet light-emitting diode (UV-LED) and a phototransistor, both fabricated in thin-film format, placed on a flexible substrate, and functionalized with biocompatible coatings, resulting in a microprobe 850 μm in width and 120 μm in thickness. The

planar configuration of the probe leads to robust mechanical stability in withstanding repeated bending while minimizing the thermal effect through efficient heat dissipation. Meanwhile, a fluorescent MOF with a favorable affinity toward dopamine is introduced, leading to excellent sensitivity and specificity with a detection limit as low as 79.9 nM. A compact flexible circuit capable of LED driving, signal processing, and wireless communication is also developed with a total weight of 0.85 g. *In vitro* characterization results have demonstrated the favorable properties and sensing performance of the probe, while *in vivo* studies suggest the great promise of the probe for detecting dopamine dynamics in living animals. Cytotoxicity testing and immunofluorescence analysis further ensure the biocompatibility of the probe for implantable applications. This work represents fundamental principles and techniques for integrating fluorescent MOFs with flexible optoelectronics for highly sensitive neurochemical sensing. By exploitation of

the structural tunability and fluorescent properties of MOFs, the combination of MOFs and flexible electronics may generate more delicate fluorescent devices with broad applications in pathological diagnosis, neuromodulation, and personalized therapy.

RESULTS AND DISCUSSION

The concept of a wireless implantable fluorescence probe mounted on the head for deep brain neurochemical sensing is illustrated in Figure 1a. The thin-film probe features an implantable needle-like structure with a UV-LED for fluorescence excitation and a phototransistor for fluorescence intensity detection. Meanwhile, based on the electrostatic interaction and energy transfer between MOFs and dopamine, europium (Eu)-based fluorescent MOFs with large surface area and high affinity toward dopamine have been synthesized and modified on the probe, enabling real-time monitoring of deep brain dopamine concentrations without aspiration of cerebrospinal fluid. The exploded view in Figure 1b represents the vertically stacked multilayer structure of the probe, whose detailed fabrication process has been illustrated in Figure S1 and Experimental Methods. The UV-LED and phototransistor were transfer-printed onto a 25-μm-thick polyimide film with prepatterned metal electrodes, followed by encapsulating with transparent SU-8 and parylene-C for electrical insulation and light transmission. The MOFs-based fluorescent film (~50 μm in thickness) covering the top of the UV-LED ensures the shielding of UV light, while the bottom graphene film (~10 μm in thickness) acts as a heat dissipation layer to prevent the probe from overheating. As a result, the probe has an overall width and thickness of 850 and 120 μm, respectively, with a length of 0.5 to 2.0 cm to accommodate different implantation depths. To diminish the overall dimensions of the device and facilitate the seamless integration of rigid semiconductor components with ultrathin flexible substrates, the UV-LEDs (510 × 510 × 195 μm^3) and phototransistors (700 × 700 × 191 μm^3) were thinned through mechanical grinding and polishing using a lapping machine (Figure S2), leading to a reduction in thickness from ~200 to ~30 μm with nanoscale roughness (Figures 1c and S3). The resulting probe can then be used for dopamine sensing based on the changes in fluorescence intensity of the MOFs under different dopamine concentrations. The UV-LED in the probe was used as a light source to excite the fluorescence of the MOF, while the phototransistor monitored changes in fluorescence intensity in real-time, resulting in a photocurrent proportional to the dopamine concentration (Figure 1d).

In addition, a miniaturized flexible circuit capable of LED driving, signal processing, and wireless communication was also developed and interfaced with the probe (Movie S1). The circuit consists of a Bluetooth Low Energy (BLE) module and peripheral integrated circuits with small footprints, all situated on a thin polyimide substrate, resulting in a lightweight highly integrated circuit 0.8 × 0.85 × 0.1 cm^3 in dimension (Figure 1e). When connected to a lithium polymer battery with a capacity of 30 mAh, the overall weight of the circuit and probe is ~0.85 g (Figure S4), leading to one of the most compact brain implants that can be easily carried by a rat without causing an excessive burden.[30−34] Anisotropic conductive film (ACF) was used as the interface between the circuit and probe to ensure mechanical and electrical stability. To facilitate device implantation, the flexible probe was endowed with temporary rigidity by encapsulating with biodegradable

polyethylene glycol (PEG), which can gradually dissolve in the cerebrospinal fluid to restore flexibility (Figure S5). The resulting probe can then be implanted into specific brain regions for fluorescence detection, while the external circuit can be mounted to the skull, enabling wireless real-time monitoring of dopamine dynamics in living animals without the requirement for bulky external equipment (Figure 1f).

Since the thinning process may degrade the device's performance, the optoelectronic properties of the ground UV-LEDs and phototransistors were first studied. The UV-LED maintained an emission of UV light at a wavelength of 283 nm after grinding, which still complied with the excitation wavelength required for the organic ligand (Figures 2a and S6). Meanwhile, no significant difference was observed in the current−voltage characteristics of the UV-LED before and after grinding (Figure 2b), indicating that the physical thinning process did not damage the epitaxial layer of the LED. The optical power was slightly attenuated under a high current, possibly due to some defects in the sapphire generated during the grinding process (Figure S7). Nonetheless, the thinned UV-LED still maintained stable light emission in both direct current (DC) and pulse modes without significant power attenuation (Figures S8 and S9). The collector characteristic curves of the thinned phototransistor show a linear response to optical power even at low intensities of 0−5 μW (Figure 2c), with a decay of 3 orders of magnitude compared to the phototransistor before grinding (Figure S10). Better optoelectronic properties may be achieved by introducing light-converging structures[35] or using customized thin-film phototransistors.[36] The probe also enables stable and reversible detection of Eu-MOF fluorescence with a relative standard deviation (RSD) of less than 0.57% under different driving currents (Figure 2d), suggesting the great reliability of the probe for real-time, continuous dopamine sensing.

The mechanical properties of the probe were later investigated to demonstrate its adaptability to soft brain tissue. Despite the deployment of rigid components, such as UV-LEDs and phototransistors, the flexible probe can withstand bending deformation at a curvature radius of 5 mm without significant performance degradation (Figure 2e). Additionally, the fatigue test with repeated bending for 500 cycles further confirmed the mechanical compatibility of the probe with soft and dynamic brain tissue (Figure 2f). Furthermore, the thermal effects of the fluorescence probe have also been explored, as excessive temperatures may cause irreversible neurological damage.[37] At an input current of 1 mA, the maximum temperature reached 39.9 °C at the LED surface when operating in a DC mode and remained below a biocompatible temperature of 38 °C in a pulsed mode (Figure 2g). As the moist environment and flowing blood in the brain may contribute to heat dissipation, further thermal analysis of the probe within biological tissue was performed by finite element simulation. A 3D model of the same size as the probe was created and surrounded by brain tissue, which contained two blood vessels 1 and 0.6 mm in diameter to mimic the brain environment (Figure S11). Due to the low luminous efficiency of UV-LEDs, the probe exhibited a temperature rise of about 0.4 to 0.8 °C on the LED surface corresponding to different pulse widths when operating at 1 mA current and 5 Hz frequency (Figure 2h). Nevertheless, the heat generated can spread rapidly along the probe through the underlying graphene heat dissipation layer (Figure S12), leading to reversible periodic changes in LED temperature without heat
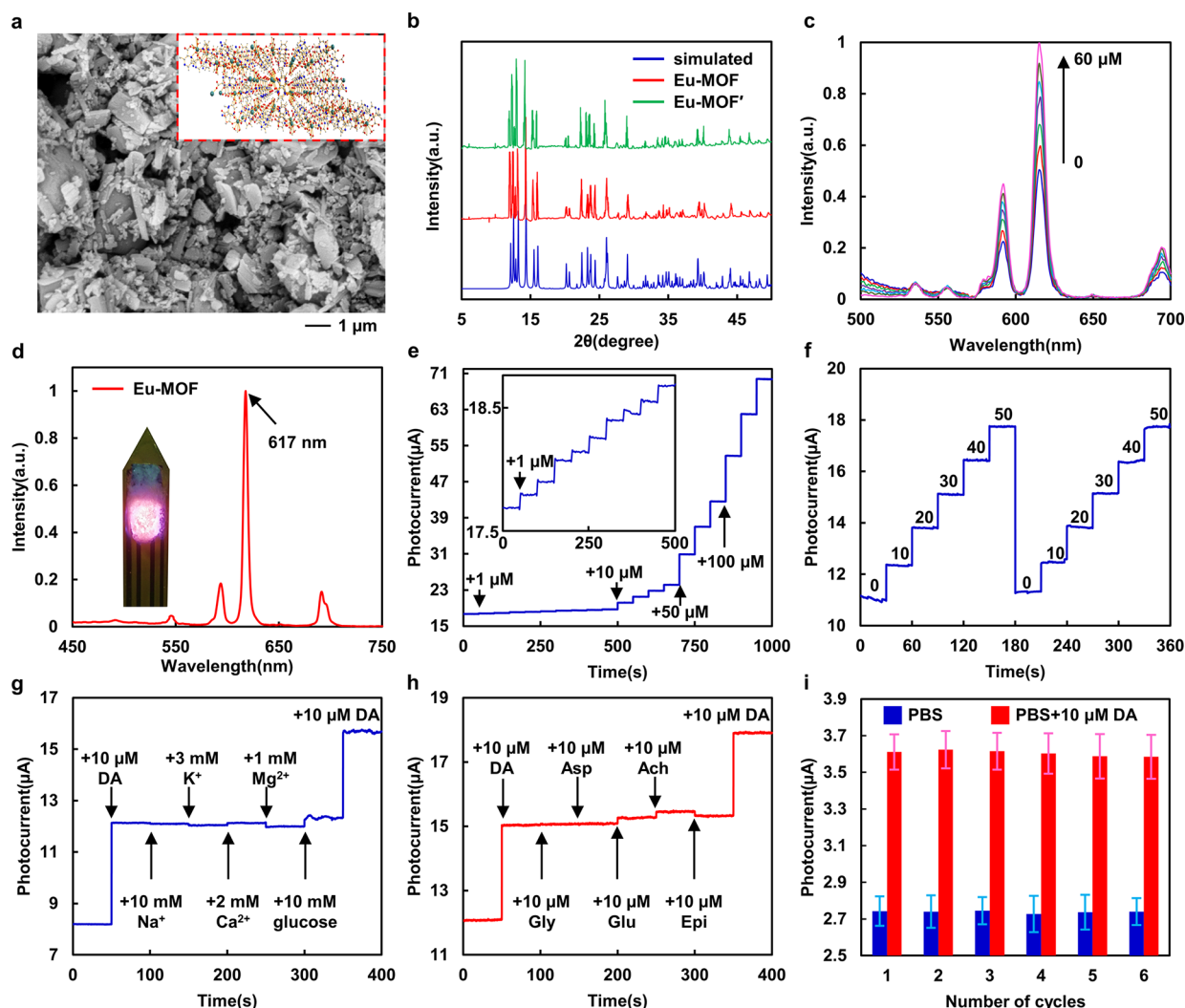
Figure 3. Sensing performance of the implantable fluorescence probe. (a) A SEM image showing the morphology of as-synthesized Eu-MOF particles. Inset: the 3D framework structure of Eu-MOF. (b) XRD patterns of the simulated result, the as-synthesized Eu-MOF, and the Eu-MOF treated with PBS for 48 h (Eu-MOF′). (c) Fluorescence intensity of Eu-MOF in PBS solutions with different dopamine concentrations. (d) The electroluminescent spectrum of the probe modified with Eu-MOF. Inset: a probe with activated red fluorescence. (e) Sensing results of the probe in PBS solutions at different dopamine concentrations. Inset: sensing results at low dopamine concentrations from 0 to 10 μM. (f) Reversibility of the probe during two cycles of dopamine sensing from 0 to 50 μM. Selectivity studies of the probe toward different (g) physiological quantities and (h) coexisting neurotransmitters. (i) Reproducibility of the probe during six consecutive cycles of the dopamine adsorption−desorption process. n = 3, error bars indicate mean $\pm$ SD.

accumulation (Figure 2i). As a result, the temperature rise at the phototransistor was consistently kept below 0.1 °C (Figure 2j), indicating that the probe can not only avoid thermal damage to the brain but also minimize the temperature drift of the phototransistor. Additionally, when the probe was operated at 2 mA, the maximum temperature of the LED reached 38.7 °C, while the temperature increase of the phototransistor was close to 0.2 °C (Figure S13). Despite the excellent intrinsic thermal properties of graphene, the inhomogeneity of the graphene layer and its tendency to delaminate during deformation can lead to high interfacial and contact thermal resistance.[38,39] Better dissipation can be achieved by incorporating hollow channels to fill and reinforce the heat dissipation material.[40] These results have demonstrated the excellent mechanical stability and tunable thermal effect of the probe, leading to favorable tissue compatibility and biosafety for deep brain applications.

The properties of the fluorescent Eu-MOF and the capability of the probe for dopamine sensing were also investigated. As-synthesized Eu-MOF particles exhibited inconsistent sizes ranging from submicron to several microns (Figure 3a), and could be downsized to the nanoscale after sonication to obtain highly uniform dispersions.[41] Powder X-ray diffraction (XRD) analysis of the simulated result, the as-synthesized Eu-MOF, and the Eu-MOF treated with phosphate-buffered saline (PBS) for 48 h (Eu-MOF') show consistent patterns with no apparent loss of major peaks (Figure 3b). Meanwhile, no significant light attenuation or peak shift in the fluorescence spectra was observed following the soaking of Eu-MOF in PBS for 24 and 48 h (Figure S14), indicating the admirable phase purity and chemical stability of the crystals in physiological environments. The capability of Eu-MOF for dopamine sensing was then verified in PBS solutions by recording fluorescence spectra at different dopamine concentrations. A significant increase in fluorescence intensity at 617 nm was observed upon increasing

Table 1. Performance Comparison to Other Implantable Dopamine Sensors

functional materials	substrate	sensing mechanism	detection limit (nM)	data transmission	reference
OPPy[a]/Nafion	silicon	electrochemical	62	wired	6
Pt/Nafion	silicon	electrochemical	200	wired	46
NPC[b]	carbon cloth	electrochemical	600	wired	47
GPCR[c]	/	fluorescent	~4	wired	48
Ln^{3+}-doped UCNPs[d]	hydrogel	fluorescent	83.6	wired	49
aptamer-graphene	polyimide	binding affinity	0.01	wired	50
glassy carbon	polyimide	electrochemical	65	wired	51
graphene/Fe$_3$O$_4$	polyimide	electrochemical	5.6	wired	52
PEDOT:PSS[e]	polyimide	electrochemical	~100	wireless	53
SWCNT/CF[f]	polyimide	electrochemical	300	wireless	54
CdSe/ZnS QDs[g]	silica	fluorescent	100	wireless	55
Eu-MOF	polyimide	fluorescent	79.9	wireless	this work

[a]Overoxidized polypyrrole. [b]N, P codoped mesoporous carbon foams. [c]G protein-coupled receptor. [d]Upconversion nanoparticles. [e]Poly(3,4-ethylenedioxythiophene) polystyrenesulfonate. [f]Single-walled carbon nanotubes-carbon fiber. [g]Quantum dots.

dopamine concentration (Figure 3c), with a correlation coefficient (R^2) of 0.9958 (Figure S15), suggesting the great prospect of Eu-MOF for discriminating dopamine in a complex interstitial fluid. To further reveal the underlying sensing mechanism, the zeta potential of Eu-MOF before and after dopamine addition was tested. The as-synthesized Eu-MOF exhibited a negative charge with a zeta potential of −14 mV (Figure S16). However, the zeta potential changed to −2 mV after the addition of dopamine, indicating the strong electrostatic interaction between Eu-MOF and positively charged dopamine.[42−44]

Subsequently, the fluorescent Eu-MOF was integrated with a miniaturized implantable probe for dopamine sensing. Due to the low dopamine concentration in brain tissue, the MOF sensing layer was placed on the outermost surface of the probe to directly interact with dopamine. To achieve effective integration of MOF particles with smooth UV-LEDs, edible beeswax with excellent biocompatibility and adhesion was embedded as a binder to form the fluorescent membrane. The modified Eu-MOF membrane exhibited bright red fluorescence with a peak wavelength of 617 nm (Figure 3d), which can be directly detected by the parallel phototransistor with a relative responsivity of 64% (Figure S17). The MOFs-modified probe was later immersed in a PBS solution with increasing dopamine concentrations. The results show that the probe responds linearly to dopamine even at low concentrations of 1 to 10 μM and tends to saturate above 200 μM (Figures 3e and S18). The limit of detection (LOD) can be calculated as follows:

$$LOD = 3.3 \times \sigma/S$$

where σ is the standard deviation of the blank measurements, and S is the slope of the calibration curve. The LOD of the probe was calculated to be 79.9 nM, comparable to that of other reported implantable microdevices (Table 1). Higher sensitivity may be further achieved by optimizing the spacing of LEDs and phototransistors or using narrow-band photodetectors that respond only to red fluorescence. In addition, an RSD of 2.73% in sensitivity with a baseline drift of 0.34 μA was observed over two sensing cycles (Figure 3f), demonstrating the great potential of the probe for reversible dopamine measurements without additional regenerative processing. The selectivity of the probe toward different physiological quantities and coexisting neurotransmitters has also been studied. The results show negligible responses to ions, glycine

(Gly), and aspartic acid (Asp), and slight responses to glucose, glutamate (Glu), and acetylcholine (Ach), with their current response being only 9.98% of that induced by dopamine (Figure 3g and 3h). Notably, the probe exhibited minimal response to epinephrine (Epi), a neurotransmitter with a molecular structure similar to that of dopamine. The excellent selectivity may be attributed not only to the strong electrostatic interactions between the MOF and dopamine molecules but also to the overlapping absorption bands between the ligand and dopamine (Figure S6), which transfers energy to Eu-MOF based on the antenna effect after UV exposure.[41,45] Furthermore, the probe demonstrates exceptional reproducibility, as evidenced by the absence of a sensitivity decay after six repeated measurements (Figure 3i). This suggests a mild and reversible adsorption−desorption process between Eu-MOF and dopamine, obviating the necessity for preconditioning and stabilization. These characterization results have demonstrated the excellent sensitivity, specificity, and stability of the implantable fluorescence probe, leading to a promising approach for real-time deep brain dopamine monitoring. It should be noted that due to differences in manually modified MOFs, structural variations such as the thickness and morphology of the MOF sensing film may affect the sensing performance of the probe. In practical use, discrepancies among probes can be further mitigated through a preset two-point calibration process.

To enable real-time *in vivo* monitoring of dopamine concentrations in living organisms, a miniaturized flexible circuit with wireless sensing capabilities was developed. The circuit contains a BLE module as a microcontroller, a constant current driver to power the UV-LED, and an amplifier to collect the photocurrent (Figure S19 and Table S1). A constant current with a maximum deviation of 3% was implemented to minimize light fluctuations of the UV-LEDs (Figure S20). The circuit exhibits favorable detection capabilities for low currents down to the nanoamp level (Figure S21), suggesting the great promise of the wireless circuit for wearable dopamine detection in freely moving subjects. The power consumption was only ~35 μA in standby mode with a current pulse of 4 mA during a Bluetooth connection event (Figure S22). To demonstrate the sensing capability of the system in real interstitial fluid environments, fresh human serum was used for dopamine sensing. The sensing results demonstrate high-fidelity measurement of dopamine in human serum samples with recoveries ranging

from 98.27% to 106.65% (Table 2), indicating potential applications of the wireless system for point-of-care detection of dopamine and diagnosis of related diseases.

Table 2. Sensing Results in Human Serum with Different Dopamine Concentrations

dopamine spiked (μM)	dopamine measured (mean ± SD, μM)	Recovery (mean ± SD, %)
1	1.01 ± 0.03	100.67 ± 2.93
2	1.97 ± 0.20	98.27 ± 9.89
3	3.07 ± 0.14	102.36 ± 4.83
4	4.29 ± 0.14	107.28 ± 3.55
5	5.32 ± 0.37	106.65 ± 7.41

The capability of the fluorescence probe for deep brain dopamine monitoring was subsequently demonstrated through a qualitative experiment conducted *in vivo* in rat brain. A MOFs-modified fluorescence probe was stereotaxically implanted into the nucleus accumbens (NAc), which is one of the primary regions that receives projections from dopaminergic neurons in the ventral tegmental area (VTA) (Figure 4a).[56] Biphasic electrical stimulations (500 μA, 20 Hz, 5 ms pulse-width) were later delivered into the VTA via a pair of stimulating electrodes to activate the VTA-NAc projection (Figure 4b). The photocurrent trace recorded by the probe exhibited low-frequency fluctuations in the dopamine concentration accompanied by intermittent spike signals (Figures 4c and S23). The low-frequency fluctuations may be attributed to dopamine homeostasis caused by spontaneous neural activity and brain feedback regulation, while the intermittent spikes
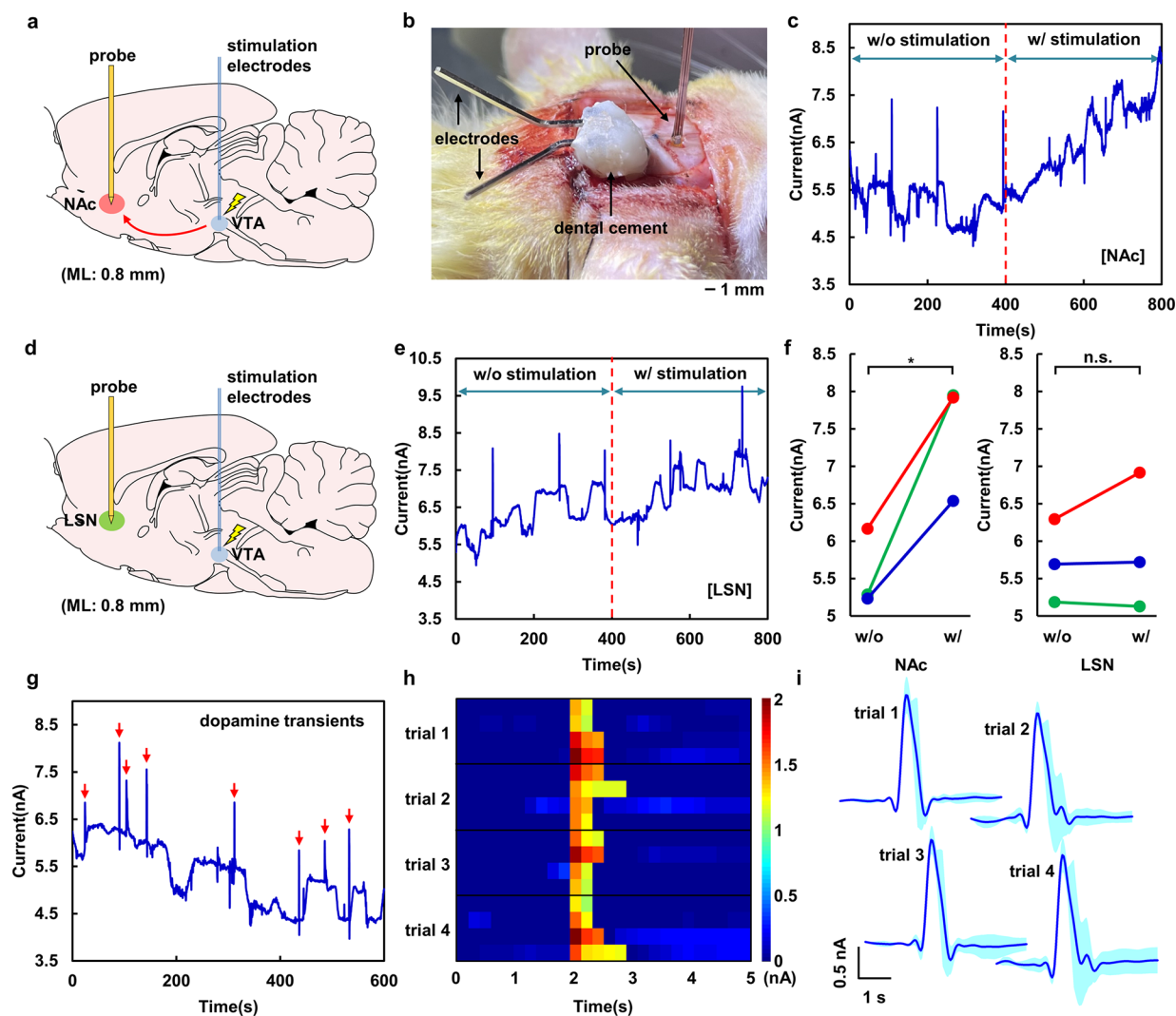

Figure 4. *In vivo* dopamine sensing using the implantable fluorescence probe. (a) Schematic of dopamine sensing in the NAc while electrically stimulating dopaminergic neurons in the VTA to activate the VTA-NAc projection. (b) An image showing a fluorescence probe and a pair of stimulating electrodes implanted and affixed to a rat brain. (c) A representative sensing result showing dopamine fluctuations in the NAc without and with continuous electrical stimulation (500 μA, 20 Hz, 5 ms pulse-width). (d) Schematic of dopamine sensing in the LSN while electrically stimulating dopaminergic neurons in the VTA. (e) A representative sensing result showing dopamine fluctuations in the LSN before and after electrical stimulation. (f) Comparison of dopamine concentration changes in NAc and LSN brain regions with and without electrical stimulation. *$p < 0.05$; n.s., not significant. (g) A representative amperometry curve measured in the NAc showing spontaneous dopamine transients. (h) Heatmaps showing the amplitude and duration of 16 spike signals from four individual trials. (i) Averaged spike signals showing consistency of dopamine transients across four trials. $n = 4$, shaded error bands indicate the mean ± SD.
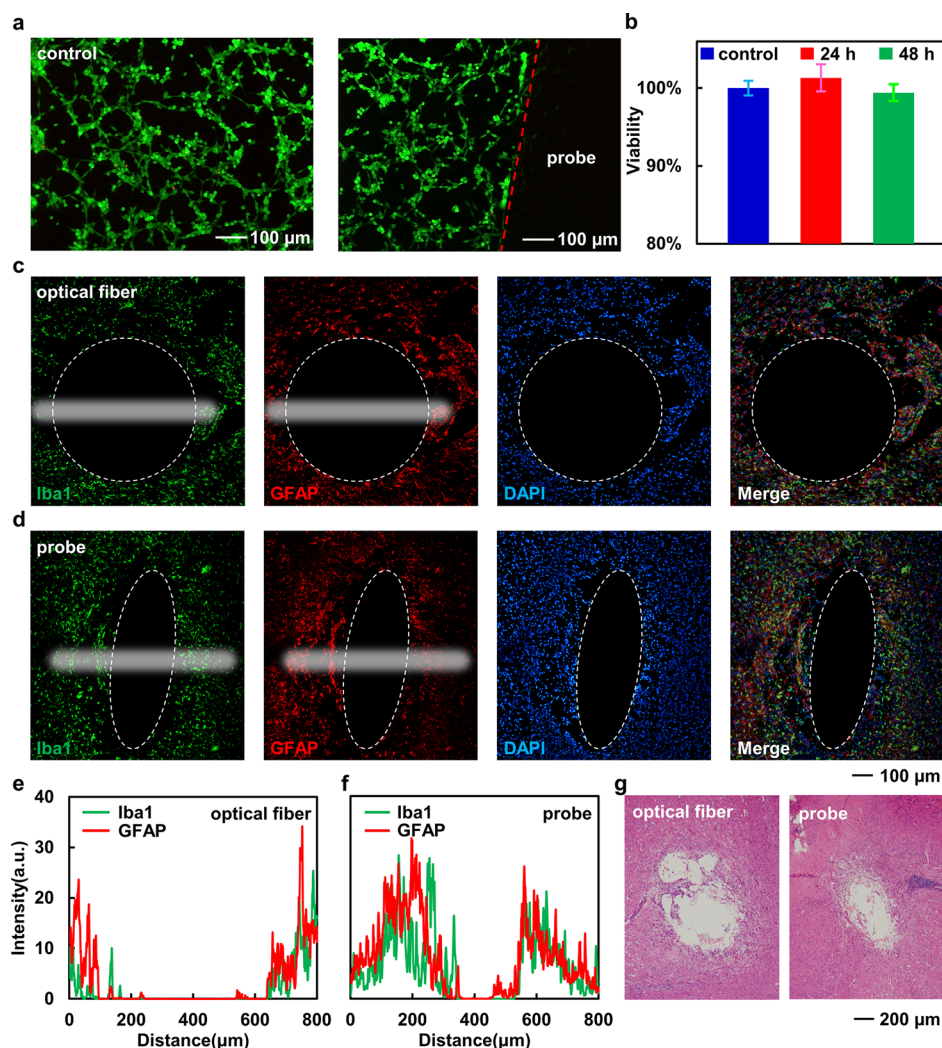
Figure 5. Biocompatibility of the implantable fluorescence probe. (a) Fluorescent images obtained by Calcein-AM/PI double-staining showing live (green) and dead (red) PC12 cells cocultured with the probe. (b) The viability of PC12 cells obtained by CCK-8 assay after culturing with the probe for 24 and 48 h, respectively. $n = 3$, error bars indicate mean $\pm$ SD. Representative immunofluorescence images of brain slices implanted with (c) an optical fiber and (d) a probe showing the distribution of surrounding microglia (Iba1, green), astrocytes (GFAP, red), and nuclei (DAPI, blue), respectively. The white lines in the image represent the areas used for quantitative analysis of inflammation. Averaged fluorescence intensity along the white lines showing the inflammatory response around (e) the optical fiber and (f) the probe, respectively. (g) H&E staining images showing the morphology of cells around the optical fiber and the probe.

may be dopamine transients released from synaptic terminals. Additionally, behaviors exhibited by rats, such as breathing and twitching, could potentially impact the relative position of brain tissue and the probe, leading to alterations in the optical path of fluorescence and fluctuations in the signals. More customized animal experiments should be performed in the future to delve deeper into this phenomenon. Notably, a dynamic increase in dopamine concentration was observed upon application of electrical stimulation, implying the promising ability of the probe to monitor dopamine dynamics during deep brain stimulation. Subsequently, another probe was implanted into the ipsilateral lateral septal nucleus (LSN) as a control to further verify the effect of neuromodulation (Figure 4d). No significant changes in dopamine concentration were observed in the LSN during electrical stimulation (Figures 4e and S24), indicating the absence of a VTA-LSN projection at this stimulation site. Comparison of dopamine concentration changes in NAc and LSN brain regions further confirmed the effective regulation of dopamine concentration

by deep brain electrical stimulation (Figure 4f), indicating the favorable performance of the fluorescence probe for real-time *in vivo* dopamine monitoring. Since the significant divergence in optical parameters between brain tissue and *in vitro* testing environments may cause the inaccuracy of pre- and/or postcalibrations, the measured sensor signals were presented instead of absolute concentrations, aligning with methodologies reported in similar research endeavors.[50,53,57,58] Further efforts, such as employing brain phantoms with similar optical parameters to brain tissue[59] or implementing *in vivo* calibration methods like microdialysis,[60] should be pursued to achieve more profound insights into dopamine dynamics. Moreover, it should also be noted that the current response of the implanted probe dropped by several orders of magnitude compared to *in vitro* experiments, possibly due to the strong absorption of visible light by brain tissue resulting in weaker fluorescence reflected to the phototransistor.[61] Enhanced sensitivity can be attained by incorporating a layer of light-guiding medium between the fluorescent film and the

phototransistor to facilitate the direct transmission of fluorescence through an internal optical path, bypassing the need to pass through brain tissue.[62,63]

In addition, the spike signals recorded by the fluorescence probe were also analyzed. A representative amperometric trace recorded in the NAc is shown in Figure 4g, where multiple spontaneous spikes were observed. Spike signals from four individual trials were then extracted, aligned, and analyzed. The results show consistent amplitudes and time constants for these spikes, matching those reported in other studies (Figure 4h and 4i),[52,53,64] indicating that the probe captures concentration transients resulting from the spontaneous release of dopamine. Moreover, the probe maintained its functionality when extracted from the brain 6 h after implantation, with an intensity decay of ~15% (Figure S25), presumably due to the nonspecific adsorption of biomolecules after device implantation. Chronic *in vivo* dopamine sensing may be achieved by introducing antibiofouling materials or self-cleaning structures to reduce the adsorption and attachment of biological substances.[65,66] These *in vivo* studies have preliminarily demonstrated the probe's capability to continuously monitor changes in dopamine levels in the deep brain, offering insights into neurotransmitter dynamics and potential mechanisms underlying related diseases. Future research may focus on conducting more quantitative experiments to refine and accurately quantify dopamine concentrations in the brain.

The biocompatibility of the implantable fluorescence probe was finally studied. Since direct exposure to UV radiation can cause degenerative changes in the cells and tissues, the UV light leakage of the probe was first evaluated. The MOF film with a thickness of about 50 μm can absorb 98% UV light. Upon increasing the thickness to 70 μm, the transmission of UV light diminished to less than 0.3%, resulting in negligible UV exposure to brain tissue (Figure S26). In addition, the UV light penetration of a 50-μm-thick MOF film under different currents was also tested (Figure S27). Even at a high current of 10 mA, the transmitted UV power was reduced from 1.76 mW to 2.12 μW after modifying the Eu-MOF membrane, leading to a power density of 7.5 μW/cm^2 that is deemed biologically safe for *in vivo* measurements.[67] Afterward, PC12 cells from transplantable rat pheochromocytomas were cocultured with the probe, followed by staining with Calcein-AM/Propidium Iodide (PI) live/dead cell double staining kit and cell counting kit-8 (CCK-8) to characterize cytotoxicity. Fluorescent images showing the distribution of live (green) and dead (red) cells indicate negligible neurotoxicity and favorable biocompatibility of the probe toward the surrounding cells (Figure 5a). Similarly, quantitative cytotoxicity tests using the CCK-8 assay also show cell viability as high as over 99% after coculture with the probe for 24 and 48 h (Figure 5b), indicating biofriendly packaging of the probe without structural collapse and material leakage. Subsequently, immunofluorescence analysis was performed to explore the neurological interaction between brain tissue and implanted probes. Commercial optical fibers (700 μm in diameter) and flexible fluorescence probes were implanted symmetrically into the two hemispheres of rat brains, which were dissected 6 weeks later and labeled with ionized calcium-binding adapter molecule 1 (Iba1) and glial fibrillary acidic protein (GFAP). The cross-sectional area of the lesion after probe implantation was around 0.202 mm^2, which is smaller than that caused by the optical fiber (Figure 5c and 5d). However, the lesion size was larger than the actual device size (~0.085 mm^2), possibly due to the tearing of the

surrounding brain tissue during implantation. Less tissue trauma may be achieved through surface-modified lubricating biocoatings or the integration of smaller optical components. In addition, the surrounding microglia and astrocytes activated by the optical fiber and the probe presented similar distributions and density without extensive deposition on the device surface (Figure 5e and 5f), indicating a favorable biocompatibility of the implantable probe comparable to commercial devices. Moreover, no obvious changes in cell morphology and structure were observed according to the hematoxylin-eosin (H&E) staining results (Figure 5g), further confirming the great biocompatibility of the flexible probe for implantable dopamine monitoring.

CONCLUSION

This work proposes materials and techniques that combine flexible optoelectronics with fluorescent MOFs to construct a miniaturized implantable probe for deep brain dopamine monitoring. The probe consists of thin-film UV-LEDs and phototransistors transfer-printed onto a flexible substrate, along with a lightweight, low-footprint wireless circuit, leading to a minimally invasive brain implant with a total weight of 0.85 g. By combining a fluorescent MOF that selectively recognizes dopamine, the probe can accurately monitor dopamine levels in the brain with a detection limit of 79.9 nM, which is comparable to conventional carbon electrodes, while delivering superior selectivity and reproducibility without consuming the analyte. In addition, the probe exhibits excellent mechanical properties and sensing stability that can adapt to complex tissue environments while enabling real-time continuous monitoring of deep brain dopamine dynamics in living animals, suggesting broad applications in uncovering neurological function and disease etiology.

The device characterization results and *in vivo* experiments have demonstrated the great prospects of MOFs-based flexible optoelectronic devices in implantable bioelectronic interfaces. By optimization of the structure of optical elements and the efficiency of fluorescent MOFs, the sensitivity and long-term stability of the probe may be further improved to enable quantitative monitoring of neurotransmitter dynamics over long periods. In addition, motion artifacts pose a significant challenge to brain implants due to the dynamic nature of brain tissue and the potential for displacement or deformation of intracranial implants. These artifacts may further be minimized by adjusting the implant angle to a noise-insensitive position[68] or by introducing engineered hydrogels as selective frequency dampers.[69] Meanwhile, more sophisticated animal experiments involving memory training, pharmacological stimulation, and social interaction must be implemented to explore the sensing performance and potential applications of the probe in complex brain environments. Furthermore, by tuning the MOF property and introducing photodetector arrays, highly integrated flexible probes capable of monitoring multiple neurochemicals simultaneously may ultimately be achieved, leading to promising solutions for neuroscience and neuropathology research.

EXPERIMENTAL METHODS

Preparation of UV-LEDs and Phototransistors. UV-LEDs (C280-PCD-10, Taihu Rootin Photoelectric display Co., Ltd.) and phototransistors (ST-0128, Opto Tech Corp.) were mechanically ground with a diamond slurry (CM-Y-200, Tianjin XiMei Technology Co., Ltd.) and polished with Alumina solution (CM-S600, Tianjin

XiMei Technology Co., Ltd.) using a precision lapping machine (UNIPOL-802, Shenyang Kejing Autoinstrument Co., Ltd.), followed by sonicating in isopropanol for 10 min to remove the residual polishing fluid. The backside of the polished phototransistors was later deposited with a Cu layer 200 nm in thickness to serve as the collector electrodes.

Synthesis of Eu-MOF. Synthesis of Eu-MOF was performed using a slow evaporation method as mentioned in a previous study.[41] Briefly, 0.17 g of H_2pzdc (P56208-25G, Sigma-Aldrich) was mixed with 25 mL of water and stirred for 5 min, after which 10 mL of 50 mM $Eu(NO_3)_3 \cdot 6H_2O$ solution (E809262, Macklin Inc.) were added and stirred for an additional 10 min. Colorless crystals were obtained at room temperature after 2 weeks. Subsequently, 5 mg of as-synthesized Eu-MOF crystals were mixed with 10 mL of water and sonicated for 30 min to obtain a highly homogeneous dispersion.

Fabrication of the Implantable Fluorescence Probe. Fabrication of the probe began with sputtering 5 nm Ti/500 nm Cu (ZhongNuo Advanced Material (Beijing) Technology Co., Ltd.) onto a polyimide thin film 25 μm in thickness (Tianjin Li Weitan Co., Ltd.), followed by photolithographically defining metal patterns to form electrodes and interconnects. The ground and polished UV-LEDs and phototransistors were then transfer-printed onto the metal electrodes using a polydimethylsiloxane (PDMS)-based stamp, followed by encapsulation with SU-8 (35 μm in thickness, SU-8 2015, Microchem Inc.) and patterning by photolithography to expose the emitter electrodes of the phototransistors. Afterward, another metal layer of 5 nm Ti/500 nm Cu was sputtered and patterned, followed by insulating with 1-μm-thick parylene-C (PDS 2010, Specialty Coating Systems Inc.). Reactive ion etching (CS-1701, Nordson MARCH Inc.) was then applied to the parylene layer, leaving only the upper surface in contact with the MOF open (approximately 480 × 480 μm^2). Subsequently, the graphene dispersion was drop-coated on the bottom of the probe and thermally deposited at 80 °C as a heat dissipation layer. Another parylene-C layer was then deposited to wrap the graphene. For the modification of Eu-MOF, a small piece of beeswax was first melted at 70 °C on the UV-LED to cover the entire upper surface of the LED, after which 1 μL of the Eu-MOF dispersion was drop-casted and deposited at 70 °C. Leveraging the hydrophobic nature of parylene, the drop-coated MOF solution remained confined within the opening, ensuring consistent MOF coating areas.

In Vitro Characterizations of the Fluorescence Probe. The surface topography of UV-LEDs and phototransistors was measured using a surface profilometer (Alpha-Step IQ, KLA Tencor Corp.). The current−voltage characteristics were obtained by a source meter (Keithley 2400, Tektronix Inc.). The optical power of UV-LEDs was quantified by a UV irradiance meter (HPL220UV-275 nm, Hangzhou Hopoo Light & Color Technology Co., Ltd.). The electroluminescent spectra of UV-LEDs and Eu-MOFs were measured by a UV spectrometer (BTC611E, B&W Tek Inc.) and a vis−NIR spectrometer (USB2000+, Ocean Optics Inc.), respectively. The absorption spectra of the organic ligand and dopamine were recorded by a UV−vis spectrophotometer (UV-2550, Shimadzu Corp.). The powder XRD patterns of Eu-MOF were obtained by a diffractometer with Cu Kα radiation (SmartLab, Rigaku Corp). The fluorescence intensities of Eu-MOF at various dopamine concentrations were measured by a fluorescence spectrophotometer (FL 6500, Perki-nElmer Inc.). To prepare the brain phantom, 5 g of gelatin (G108398, Aladdin Biochemical Technology Co., Ltd.) were dissolved into 100 mL of water and stirred at 70 °C for 30 min, followed by curing in a rubber-based brain impression at 4 °C overnight. Thermal measurements were performed using a thermal imaging camera (226s, FOTRIC Inc.) at a background temperature of 37 °C.

Thermal Modeling. Finite element analysis was performed using the software COMSOL Multiphysics 6.0 (COMSOL Inc.). A 3D model that is consistent with the actual device dimensions was created for thermal modeling. The probe was wrapped in brain tissue with two blood vessels 1 and 0.6 mm in diameter, respectively. Heat transfer in biological tissue is governed by Penne's formula as follows:

$$\rho C_p \frac{\partial T}{\partial t} + \nabla \cdot q = \rho_b C_{p,b} \omega_b (T_b - T) + Q$$

$$q = -k\nabla T$$

where ρ is the brain density (1040 kg/m^3), C_p is the specific heat capacity of the brain (3650 J/(kg·K)), k is the brain thermal conductivity (0.45 W/(m·K)), ρ_b is the blood density (1000 kg/m^3), $C_{p,b}$ is the specific heat capacity of the blood (4180 J/(kg·K)), ω_b is the blood perfusion rate (0.0064 1/s), T_b is the blood temperature (37 °C), and Q is the LED heat source. For the UV-LED, the density, heat capacity, and thermal conductivity are 2330 kg/m^3, 700 J/(kg·K), and 230 W/(m·K), respectively. For the phototransistor, the density, heat capacity, and thermal conductivity are 2329 kg/m^3, 700 J/(kg·K), and 130 W/(m·K), respectively. For graphene, the density, heat capacity, and thermal conductivity are 2267 kg/m^3, 1000 J/(kg·K), and 2300 W/(m·K), respectively. The heat source Q is defined based on the wall-plug efficiency of the UV-LED. The initial temperature is set as 37 °C.

Design of the Wireless Flexible Circuit. The wireless circuit consists of a BLE module with an embedded antenna (EYSNSNZWW, Taiyo Yuden Co., Ltd.), a low-dropout voltage regulator (LP5907UVX-3.3/NOPB, Texas Instruments Inc.), a constant current LED driver (TPS61042DRBRG4, Texas Instruments Inc.), and a micropower low-noise amplifier (ADA4505-1ACBZ-R7, Analog Devices, Inc.), all of which were placed on a thin polyimide substrate with prepatterned copper interconnects. The circuit was powered by a rechargeable lithium polymer battery with a capacity of 30 mAh (301012, Shenzhen Bihuade Technology Co., Ltd.). 1-μm-thick parylene C was deposited on the circuit for electrical insulation and waterproofing, after which a fluorescence probe was connected to the circuit using ACF tape (PAF700D, Dexerials Corp.).

In Vivo Dopamine Measurements. All animal experiments and procedures were performed with the approval of the Ethics Committee of Zhejiang University. Sprague−Dawley rats (male, 300−350 g, Zhejiang Academy of Medical Sciences) were anesthetized by intraperitoneal injection of propofol and then fixed on a stereotaxic apparatus, after which the scalp was incised to expose the skull. Afterward, the holes in the skull were opened with a cranial drill, and the underlying dura mater was punctured with a syringe needle to facilitate device implantation. A pair of stimulating electrodes were implanted into the VTA at an angle of 20° (converted coordinates from bregma: −5.2 anteroposterior (AP), 3.91 medio-lateral (ML), −8.51 mm dorsoventral (DV)), followed by fixing to the skull using dental cement. To avoid device bending during implantation, the probe was coated with biodissolvable PEG (81268-250 g, Sigma-Aldrich Corp.) as a temporary stiffener before implantation. The PEG coating can gradually dissolve in the cerebrospinal fluid within minutes of implantation without affecting the flexibility and functionality of the probe. Subsequently, PEG-coated flexible probes were affixed to the arm of the stereotaxic apparatus and implanted into NAc (1.7 AP, 0.8 ML, −7.2 DV) and LSN (1.7 AP, 0.8 ML, −6.0 DV), respectively. The implanted probes were allowed to operate without electrical stimulation for at least 5 min before each test to stabilize the baseline. Biphasic electrical pulses (500 μA, 20 Hz, 5 ms pulse-width) were then generated by a constant current stimulator system (PlexStim, Plexon Inc.) and delivered into the VTA, while the corresponding dopamine dynamics were recorded by the probes in the NAc and LSN, respectively. The entire test duration was 800 s, in which pulsed electrical stimulation was continuously applied in the second half of the period (400 s).

Cytotoxicity Tests. Cytotoxicity tests were performed using live/dead cell double-staining reagent and CCK-8 reagent, respectively. The probes were first sterilized under UV light overnight, followed by coculturing with PC12 cells (Nanjing Cobioer Biosciences Co., Ltd.) in an atmosphere of 37 °C, 95% air, and 5% CO$_2$. For the double-staining assay, Calcein-AM (C2012-0.1 mL, Sigma-Aldrich Corp.) and PI (C81854-25MG, Sigma-Aldrich Corp.) were used to stain the live and dead cells after 24 h of coculture. Fluorescent images showing the distribution of live and dead cells were obtained by a fluorescence

microscope (IX73, Olympus, Corp.). For the CCK-8 assay, 10 μL of CCK-8 solution (CK04, Dojindo Molecular Technologies, Inc.) were added to the samples after 24 and 48 h of coculture, respectively, followed by an additional 2 h of incubation. The cytotoxicity was characterized by measuring the absorbance of the culture medium at 450 nm with a microplate reader (Multiskan FC, Thermo Fisher Scientific Inc.).

Immunofluorescence and Imaging. Rats were anesthetized with isoflurane and subsequently intracardially perfused with a 0.9% NaCl solution followed by 4% paraformaldehyde in 0.1 M phosphate buffer. Brains were dissected, washed three times with PBS, and further fixed in 4% paraformaldehyde for 24 h at 4 °C. The brain slices (10 μm in thickness) at the tip of the device were later dissected, cleaned, and blocked in a solution containing 1X PBS, 5% normal goat serum, and 0.3% Triton X-100 for 1 h. Afterward, brain slices were incubated in a buffer containing anti-Iba1 antibody (1:200, Rabbit, ab178846, Abcam PLC.) and anti-GFAP antibody (1:500, Mouse, 60190-1-lg, Proteintech Group Inc.,) overnight at 4 °C. Subsequently, brain slices were rinsed three times for 5 min each in PBS and incubated in buffer containing goat antirabbit IgG Alexa Fluor 488 (1:200, ab150077, Abcam PLC.) and goat antimouse IgG Alexa Fluor 647 (1:200, ab150115, Abcam PLC.) for 1 h at room temperature. After washing three times with PBS, the brain slices were finally stained with 4′,6-diamidino-2-phenylindole (DAPI, AR1176, Boster Biological Technology Co., Ltd.) for 1 h. Fluorescent images were captured with an inverted microscope (IX73, Olympus, Corp.).

Statistical Analysis. Statistical analysis was performed by using Microsoft Excel software (Microsoft Corp.). All statistical data were obtained from at least three independent replicates and were expressed as the mean $\pm$ standard deviation (SD). Paired samples t-test was used to analyze statistically significant differences. $*p < 0.05$; n.s., not significant.

ASSOCIATED CONTENT

ⓈI Supporting Information

The Supporting Information is available free of charge at https://pubs.acs.org/doi/10.1021/acsnano.4c00632.

> Figures S1−S27, Table S1: the detailed fabrication process of the probe; additional characterization (surface roughness, absorption spectra, wall-plug efficiency, collector characteristic) and thermal simulation of the probe; design and characterization of the flexible circuit; continuous *in vivo* testing results of dopamine concentrations (PDF)

> Movie S1: A wireless flexible circuit with programmable fluorescence excitation and sensing capabilities (MP4)

AUTHOR INFORMATION

Corresponding Authors

Tao Tang − *Research Center for Augmented Intelligence, Research Institute of Artificial Intelligence, Zhejiang Lab, Hangzhou 311121, China*; Email: tangt@zhejianglab.com

Xian Huang − *School of Precision Instrument and Optoelectronics Engineering, Tianjin University, Tianjin 300072, China; State Key Laboratory of Precision Measuring Technology and Instruments, Tianjin University, Tianjin 300072, China; Center of Flexible Wearable Technology, Institute of Flexible Electronic Technology of Tsinghua, Jiaxing 314006, China;* ⓸ orcid.org/0000-0002-8788-9185; Email: huangxian@tju.edu.cn

Authors

Wei Ling − *Research Center for Augmented Intelligence, Research Institute of Artificial Intelligence, Zhejiang Lab, Hangzhou 311121, China; School of Precision Instrument*

and Optoelectronics Engineering, Tianjin University, Tianjin 300072, China; ⓸ orcid.org/0000-0002-2544-5650

Xue Shang − *Research Center for Intelligent Sensing Systems, Research Institute of Intelligent Sensing, Zhejiang Lab, Hangzhou 311121, China;* ⓸ orcid.org/0009-0001-4895-2604

Chaonan Yu − *Nanhu Brain-computer Interface Institute, Hangzhou 311100, China*

Chenxi Li − *State Key Laboratory of Precision Measuring Technology and Instruments, Tianjin University, Tianjin 300072, China*

Kedi Xu − *Nanhu Brain-computer Interface Institute, Hangzhou 311100, China; Key Laboratory of Biomedical Engineering of Education Ministry, Department of Biomedical Engineering, Zhejiang University, Hangzhou 310027, China*

Linqing Feng − *Research Center for Augmented Intelligence, Research Institute of Artificial Intelligence, Zhejiang Lab, Hangzhou 311121, China*

Yina Wei − *Research Center for Augmented Intelligence, Research Institute of Artificial Intelligence, Zhejiang Lab, Hangzhou 311121, China*

Complete contact information is available at:
https://pubs.acs.org/10.1021/acsnano.4c00632

Author Contributions

○W.L. and X.S. contributed equally to this work. W.L. and X.S. designed and fabricated the device. X.S. synthesized the Eu-MOF. W.L., X.S., and C.L. performed the *in vitro* characterization. W.L. and T.T. designed and prepared the circuit. W.L. and X.S. carried out the simulation. C.Y. performed the *in vivo* measurements. X.H. conceived, designed, and supervised the project. W.L., T.T., and X.H. prepared the manuscript. All authors discussed the results and commented on the manuscript.

Notes

The authors declare no competing financial interest.

ACKNOWLEDGMENTS

REFERENCES

(1) Kavalali, E. T. The Mechanisms and Functions of Spontaneous Neurotransmitter Release. *Nat. Rev. Neurosci.* **2015**, *16*, 5−16.

(2) Watson, C. J.; Venton, B. J.; Kennedy, R. T. In Vivo Measurements of Neurotransmitters by Microdialysis Sampling. *Anal. Chem.* **2006**, *78*, 1391−1399.

(3) Ceccarini, J.; Liu, H.; Van Laere, K.; Morris, E. D.; Sander, C. Y. Methods for Quantifying Neurotransmitter Dynamics in the Living Brain with PET Imaging. *Front. physiol.* **2020**, *11*, 792.

(4) Payne, T. D.; Moody, A. S.; Wood, A. L.; Pimiento, P. A.; Elliott, J. C.; Sharma, B. Raman Spectroscopy and Neuroscience: From

Fundamental Understanding to Disease Diagnostics and Imaging. *Analyst* **2020**, *145*, 3461−3480.

(5) Moldovan, N.; Blaga, I.-I.; Billa, S.; Hossain, I.; Gong, C.; Jones, C. E.; Murray, T. A.; Divan, R.; Siddiqui, S.; Arumugam, P. U. Brain-Implantable Multifunctional Probe for Simultaneous Detection of Glutamate and GABA Neurotransmitters. *Sens. Actuators B: Chem.* **2021**, *337*, 129795.

(6) Tseng, T. T. C.; Monbouquette, H. G. Implantable Microprobe with Arrayed Microsensors for Combined Amperometric Monitoring of the Neurotransmitters, Glutamate and Dopamine. *J. Electroanal. Chem.* **2012**, *682*, 141−146.

(7) Zhou, Y.; Liu, B.; Lei, Y.; Tang, L.; Li, T.; Yu, S.; Zhang, G.-J.; Li, Y.-T. Acupuncture Needle-Based Transistor Neuroprobe for In Vivo Monitoring of Neurotransmitter. *Small* **2022**, *18*, 2204142.

(8) Mariani, F.; Quast, T.; Andronescu, C.; Gualandi, I.; Fraboni, B.; Tonelli, D.; Scavetta, E.; Schuhmann, W. Needle-Type Organic Electrochemical Transistor for Spatially Resolved Detection of Dopamine. *Microchim. Acta* **2020**, *187*, 378.

(9) Pisano, F.; Pisanello, M.; Lee, S. J.; Lee, J.; Maglie, E.; Balena, A.; Sileo, L.; Spagnolo, B.; Bianco, M.; Hyun, M.; De Vittorio, M.; Sabatini, B. L.; Pisanello, F. Depth-Resolved Fiber Photometry with a Single Tapered Optical Fiber Implant. *Nat. Methods* **2019**, *16*, 1185−1192.

(10) Zheng, D.; Pisano, F.; Collard, L.; Balena, A.; Pisanello, M.; Spagnolo, B.; Mach-Batlle, R.; Tantussi, F.; Carbone, L.; De Angelis, F.; Valiente, M.; de la Prida, L. M.; Ciracì, C.; De Vittorio, M.; Pisanello, F. Toward Plasmonic Neural Probes: SERS Detection of Neurotransmitters through Gold-Nanoislands-Decorated Tapered Optical Fibers with Sub-10 nm Gaps. *Adv. Mater.* **2023**, *35*, 2200902.

(11) Tang, X.; Shen, H.; Zhao, S.; Li, N.; Liu, J. Flexible Brain-Computer Interfaces. *Nat. Electron.* **2023**, *6*, 109−118.

(12) Ling, W.; Yu, J.; Ma, N.; Li, Y.; Wu, Z.; Liang, R.; Hao, Y.; Pan, H.; Liu, W.; Fu, B.; Wang, K.; Wang, H.; Li, L.; Sheng, X.; Peng, H.; Ning, B.; Yang, J.; Huang, X. Flexible Electronics and Materials for Synchronized Stimulation and Monitoring in Multi-Encephalic Regions. *Adv. Funct. Mater.* **2020**, *30*, 2002644.

(13) Zhang, S.; Chhetry, A.; Zahed, M. A.; Sharma, S.; Park, C.; Yoon, S.; Park, J. Y. On-Skin Ultrathin and Stretchable Multifunctional Sensor for Smart Healthcare Wearables. *npj Flexible Electron.* **2022**, *6*, 11.

(14) Wan, C.; Wu, Z.; Ren, M.; Tang, M.; Gao, Y.; Shang, X.; Li, T.; Xia, Z.; Yang, Z.; Mao, S.; Zhou, M.; Ling, W.; Li, J.; Huo, W.; Huang, X. In Situ Formation of Conductive Epidermal Electrodes Using a Fully Integrated Flexible System and Injectable Photocurable Ink. *ACS Nano* **2023**, *17*, 10689−10700.

(15) Ling, W.; Wang, Y.; Lu, B.; Shang, X.; Wu, Z.; Chen, Z.; Li, X.; Zou, C.; Yan, J.; Zhou, Y.; Liu, J.; Li, H.; Que, K.; Huang, X. Continuously Quantifying Oral Chemicals Based on Flexible Hybrid Electronics for Clinical Diagnosis and Pathogenetic Study. *Research* **2022**, *2022*, 9810129.

(16) Gao, Y.; Nguyen, D. T.; Yeo, T.; Lim, S. B.; Tan, W. X.; Madden, L. E.; Jin, L.; Long, J. Y. K.; Aloweni, F. A. B.; Liew, Y. J. A.; Tan, M. L. L.; Ang, S. Y.; Maniya, S. D. O.; Abdelwahab, I.; Loh, K. P.; Chen, C.-H.; Becker, D. L.; Leavesley, D.; Ho, J. S.; Lim, C. T. A Flexible Multiplexed Immunosensor for Point-of-Care In Situ Wound Monitoring. *Sci. Adv.* **2021**, *7*, No. eabg9614.

(17) Zhao, C.; Man, T.; Cao, Y.; Weiss, P. S.; Monbouquette, H. G.; Andrews, A. M. Flexible and Implantable Polyimide Aptamer-Field-Effect Transistor Biosensors. *ACS Sens.* **2022**, *7*, 3644−3653.

(18) He, J.; Spanolios, E.; Froehlich, C. E.; Wouters, C. L.; Haynes, C. L. Recent Advances in the Development and Characterization of Electrochemical and Electrical Biosensors for Small Molecule Neurotransmitters. *ACS Sens.* **2023**, *8*, 1391−1403.

(19) Fan, R.; Andrew, T. L. Perspective-Challenges in Developing Wearable Electrochemical Sensors for Longitudinal Health Monitoring. *J. Electrochem. Soc.* **2020**, *167*, 037542.

(20) Zhang, Y.; Jiang, N.; Yetisen, A. K. Brain Neurochemical Monitoring. *Biosens. Bioelectron.* **2021**, *189*, 113351.

(21) Zhang, Y.; Hu, Y.; Liu, Q.; Lou, K.; Wang, S.; Zhang, N.; Jiang, N.; Yetisen, A. K. Multiplexed Optical Fiber Sensors for Dynamic Brain Monitoring. *Matter* **2022**, *5*, 3947−3976.

(22) Chen, M.; He, Y.; Liang, H.; Zhou, H.; Wang, X.; Heng, X.; Zhang, Z.; Gan, J.; Yang, Z. Stretchable and Strain-Decoupled Fluorescent Optical Fiber Sensor for Body Temperature and Movement Monitoring. *ACS Photonics* **2022**, *9*, 1415−1424.

(23) Jung, Y. H.; Kim, J. U.; Lee, J. S.; Shin, J. H.; Jung, W.; Ok, J.; Kim, T.-i. Injectable Biomedical Devices for Sensing and Stimulating Internal Body Organs. *Adv. Mater.* **2020**, *32*, 1907478.

(24) Kim, T.-i.; McCall, J. G.; Jung, Y. H.; Huang, X.; Siuda, E. R.; Li, Y.; Song, J.; Song, Y. M.; Pao, H. A.; Kim, R.-H.; Lu, C.; Lee, S. D.; Song, I.-S.; Shin, G.; Al-Hasani, R.; Kim, S.; Tan, M. P.; Huang, Y.; Omenetto, F. G.; Rogers, J. A.; et al. Injectable, Cellular-Scale Optoelectronics with Applications for Wireless Optogenetics. *Science* **2013**, *340*, 211−216.

(25) Furukawa, H.; Cordova, K. E.; O'Keeffe, M.; Yaghi, O. M. The Chemistry and Applications of Metal-Organic Frameworks. *Science* **2013**, *341*, 1230444.

(26) Ling, W.; Liew, G.; Li, Y.; Hao, Y.; Pan, H.; Wang, H.; Ning, B.; Xu, H.; Huang, X. Materials and Techniques for Implantable Nutrient Sensing Using Flexible Sensors Integrated with Metal-Organic Frameworks. *Adv. Mater.* **2018**, *30*, 1800917.

(27) Ling, W.; Hao, Y.; Wang, H.; Xu, H.; Huang, X. A Novel Cu-Metal-Organic Framework with Two-Dimensional Layered Topology for Electrochemical Detection Using Flexible Sensors. *Nanotechnology* **2019**, *30*, 424002.

(28) Yang, X.; Yi, J.; Wang, T.; Feng, Y.; Wang, J.; Yu, J.; Zhang, F.; Jiang, Z.; Lv, Z.; Li, H.; Huang, T.; Si, D.; Wang, X.; Cao, R.; Chen, X. Wet-Adhesive On-Skin Sensors Based on Metal-Organic Frameworks for Wireless Monitoring of Metabolites in Sweat. *Adv. Mater.* **2022**, *34*, 2201768.

(29) Shu, Y.; Shang, Z.; Su, T.; Zhang, S.; Lu, Q.; Xu, Q.; Hu, X. A Highly Flexible Ni-Co MOF Nanosheet Coated Au/PDMS Film Based Wearable Electrochemical Sensor for Continuous Human Sweat Glucose Monitoring. *Analyst* **2022**, *147*, 1440−1448.

(30) Kim, C. Y.; Ku, M. J.; Qazi, R.; Nam, H. J.; Park, J. W.; Nam, K. S.; Oh, S.; Kang, I.; Jang, J.-H.; Kim, W. Y.; Kim, J.-H.; Jeong, J.-W. Soft Subdermal Implant Capable of Wireless Battery Charging and Programmable Controls for Applications in Optogenetics. *Nat. Commun.* **2021**, *12*, 535.

(31) Burton, A.; Won, S. M.; Sohrabi, A. K.; Stuart, T.; Amirhossein, A.; Kim, J. U.; Park, Y.; Gabros, A.; Rogers, J. A.; Vitale, F.; Richardson, A. G.; Gutruf, P. Wireless, Battery-Free, and Fully Implantable Electrical Neurostimulation in Freely Moving Rodents. *Microsyst. Nanoeng.* **2021**, *7*, 62.

(32) Zhang, Y.; Castro, D. C.; Han, Y.; Wu, Y.; Guo, H.; Weng, Z.; Xue, Y.; Ausra, J.; Wang, X.; Li, R.; Wu, G.; Vázquez-Guardado, A.; Xie, Y.; Xie, Z.; Ostojich, D.; Peng, D.; Sun, R.; Wang, B.; Yu, Y.; Leshock, J. P.; et al. Battery-Free, Lightweight, Injectable Microsystem for In Vivo Wireless Pharmacology and Optogenetics. *Proc. Natl. Acad. Sci. U. S. A.* **2019**, *116*, 21427−21437.

(33) Li, L.; Lu, L.; Ren, Y.; Tang, G.; Zhao, Y.; Cai, X.; Shi, Z.; Ding, H.; Liu, C.; Cheng, D.; Xie, Y.; Wang, H.; Fu, X.; Yin, L.; Luo, M.; Sheng, X. Colocalized, Bidirectional Optogenetic Modulations in Freely Behaving Mice with a Wireless Dual-Color Optoelectronic Probe. *Nat. Commun.* **2022**, *13*, 839.

(34) Shang, X.; Ling, W.; Chen, Y.; Li, C.; Huang, X. Construction of a Flexible Optogenetic Device for Multisite and Multiregional Optical Stimulation Through Flexible μ-LED Displays on the Cerebral Cortex. *Small* **2023**, *19*, 2302241.

(35) Kobayashi, K.; Kan, T. S/N Improvement of Nano-Cuboid Photodetector Using Combination of Small Device Area and Converging Lens. In *2020 IEEE 33rd International Conference on Micro Electro Mechanical Systems (MEMS)*, 18−22 Jan. 2020, 2020; pp 1163−1166.

(36) Yoo, H.; Kim, W.-G.; Kang, B. H.; Kim, H. T.; Park, J. W.; Choi, D. H.; Kim, T. S.; Lim, J. H.; Kim, H. J. High Photosensitive Indium-Gallium-Zinc Oxide Thin-Film Phototransistor with a

Selenium Capping Layer for Visible-Light Detection. *ACS Appl. Mater. Interfaces* **2020**, *12*, 10673−10680.

(37) Walter, E. J.; Carraretto, M. The Neurological and Cognitive Consequences of Hyperthermia. *Crit. Care* **2016**, *20*, 199.

(38) Yang, G.; Yi, H.; Yao, Y.; Li, C.; Li, Z. Thermally Conductive Graphene Films for Heat Dissipation. *ACS Appl. Nano Mater.* **2020**, *3*, 2149−2155.

(39) Pop, E.; Varshney, V.; Roy, A. K. Thermal Properties of Graphene: Fundamentals and Applications. *MRS Bull.* **2012**, *37*, 1273−1281.

(40) Lee, J. S.; Choi, J.; Park, G. Y.; Kang, S. J.; Yang, J.-h.; Lee, Y.; Choi, M.; Kim, K.; Kim, T.-i. Thermally Managed, Injectable Optoelectronic Probe with Heat Dissipation Guide for Photodynamic Therapy. *Small* **2023**, *19*, 2300753.

(41) Moghzi, F.; Soleimannejad, J.; Sañudo, E. C.; Janczak, J. Dopamine Sensing Based on Ultrathin Fluorescent Metal-Organic Nanosheets. *ACS Appl. Mater. Interfaces* **2020**, *12*, 44499−44507.

(42) Pang, Y.; Cao, Y.; Han, J.; Xia, Y.; He, Z.; Sun, L.; Liang, J. A Novel Fluorescence Sensor Based on Zn Porphyrin MOFs for the Detection of Bisphenol A with Highly Selectivity and Sensitivity. *Food Control* **2022**, *132*, 108551.

(43) Cheng, Y.; Wu, J.; Guo, C.; Li, X.-G.; Ding, B.; Li, Y. A Facile Water-Stable MOF-Based "Off-On" Fluorescent Switch for Label-Free Detection of Dopamine In Biological Fluid. *J. Mater. Chem. B* **2017**, *5*, 2524−2535.

(44) Zhang, J.; Xu, X.; Chen, L. An Ultrasensitive Electrochemical Bisphenol A Sensor Based on Hierarchical Ce-Metal-Organic Framework Modified with Cetyltrimethylammonium Bromide. *Sens. Actuators B: Chem.* **2018**, *261*, 425−433.

(45) Wu, S.; Lin, Y.; Liu, J.; Shi, W.; Yang, G.; Cheng, P. Rapid Detection of the Biomarkers for Carcinoid Tumors by a Water Stable Luminescent Lanthanide Metal-Organic Framework Sensor. *Adv. Funct. Mater.* **2018**, *28*, 1707169.

(46) Johnson, M. D.; Franklin, R. K.; Gibson, M. D.; Brown, R. B.; Kipke, D. R. Implantable Microelectrode Arrays for Simultaneous Electrophysiological and Neurochemical Recordings. *J. Neurosci. Methods* **2008**, *174*, 62−70.

(47) Zhao, L.; Cai, Z.; Yao, Q.; Zhao, T.; Lin, H.; Xiao, Y.; Chen, X. Electropolymerization Fabrication of Three-Dimensional N, P-Co-Doped Carbon Network as a Flexible Electrochemical Dopamine Sensor. *Sens. Actuators B: Chem.* **2017**, *253*, 1113−1119.

(48) Sun, F.; Zhou, J.; Dai, B.; Qian, T.; Zeng, J.; Li, X.; Zhuo, Y.; Zhang, Y.; Wang, Y.; Qian, C.; Tan, K.; Feng, J.; Dong, H.; Lin, D.; Cui, G.; Li, Y. Next-Generation Grab Sensors for Monitoring Dopaminergic Activity In Vivo. *Nat. Methods* **2020**, *17*, 1156−1166.

(49) Zhou, B.; Guo, J.; Yang, C.; Kong, L. Upconversion-Luminescent Hydrogel Optical Probe for In Situ Dopamine Monitoring. *Photonics Res.* **2020**, *8*, 1800−1807.

(50) Wu, G.; Zhang, N.; Matarasso, A.; Heck, I.; Li, H.; Lu, W.; Phaup, J. G.; Schneider, M. J.; Wu, Y.; Weng, Z.; Sun, H.; Gao, Z.; Zhang, X.; Sandberg, S. G.; Parvin, D.; Seaholm, E.; Islam, S. K.; Wang, X.; Phillips, P. E. M.; Castro, D. C.; et al. Implantable Aptamer-Graphene Microtransistors for Real-Time Monitoring of Neurochemical Release In Vivo. *Nano Lett.* **2022**, *22*, 3668−3677.

(51) VanDersarl, J. J.; Mercanzini, A.; Renaud, P. Integration of 2D and 3D Thin Film Glassy Carbon Electrode Arrays for Electrochemical Dopamine Sensing in Flexible Neuroelectronic Implants. *Adv. Funct. Mater.* **2015**, *25*, 78−84.

(52) Li, J.; Liu, Y.; Yuan, L.; Zhang, B.; Bishop, E. S.; Wang, K.; Tang, J.; Zheng, Y.-Q.; Xu, W.; Niu, S.; Beker, L.; Li, T. L.; Chen, G.; Diyaolu, M.; Thomas, A.-L.; Mottini, V.; Tok, J. B. H.; Dunn, J. C. Y.; Cui, B.; Paşca, S. P.; et al. A Tissue-Like Neurotransmitter Sensor for the Brain and Gut. *Nature* **2022**, *606*, 94−101.

(53) Liu, C.; Zhao, Y.; Cai, X.; Xie, Y.; Wang, T.; Cheng, D.; Li, L.; Li, R.; Deng, Y.; Ding, H.; Lv, G.; Zhao, G.; Liu, L.; Zou, G.; Feng, M.; Sun, Q.; Yin, L.; Sheng, X. A Wireless, Implantable Optoelectrochemical Probe for Optogenetic Stimulation and Dopamine Detection. *Microsyst. Nanoeng.* **2020**, *6*, 64.

(54) Stuart, T.; Jeang, W. J.; Slivicki, R. A.; Brown, B. J.; Burton, A.; Brings, V. E.; Alarcón-Segovia, L. C.; Agyare, P.; Ruiz, S.; Tyree, A.; Pruitt, L.; Madhvapathy, S.; Niemiec, M.; Zhuang, J.; Krishnan, S.; Copits, B. A.; Rogers, J. A.; Gereau, R. W. I. V.; Samineni, V. K.; Bandodkar, A. J.; et al. Wireless, Battery-Free Implants for Electrochemical Catecholamine Sensing and Optogenetic Stimulation. *ACS Nano* **2023**, *17*, 561−574.

(55) Kim, M. H.; Yoon, H.; Choi, S. H.; Zhao, F.; Kim, J.; Song, K. D.; Lee, U. Miniaturized and Wireless Optical Neurotransmitter Sensor for Real-Time Monitoring of Dopamine in the Brain. *Sensors* **2016**, *16*, 1894.

(56) Wang, R. Y. Dopaminergic Neurons in the Rat Ventral Tegmental Area. I. Identification and Characterization. *Brain Res. Rev.* **1981**, *3*, 123−140.

(57) Jung, H. H.; Ha, J.; Park, J.; Kang, S.; Kim, J.; Jung, H. N.; Kim, S.; Yea, J.; Lee, H.; Oh, S.; Jekal, J.; Song, S.; Son, J.; Yu, T. S.; Lee, Y.; Won, J.; Lim, K. S.; Lee, Y. K.; Keum, H.; Lee, T.; et al. Highly Deformable Double-Sided Neural Probe with All-in-One Electrode System for Real-Time In Vivo Detection of Dopamine for Parkinson's Disease. *Adv. Funct. Mater.* **2024**, *34*, 2311436.

(58) Sun, F.; Zeng, J.; Jing, M.; Zhou, J.; Feng, J.; Owen, S. F.; Luo, Y.; Li, F.; Wang, H.; Yamaguchi, T.; Yong, Z.; Gao, Y.; Peng, W.; Wang, L.; Zhang, S.; Du, J.; Lin, D.; Xu, M.; Kreitzer, A. C.; Cui, G.; et al. A Genetically Encoded Fluorescent Sensor Enables Rapid and Specific Detection of Dopamine in Flies, Fish, and Mice. *Cell* **2018**, *174*, 481−496.e419.

(59) Ntombela, L.; Adeleye, B.; Chetty, N. Low-Cost Fabrication of Optical Tissue Phantoms for Use in Biomedical Imaging. *Heliyon* **2020**, *6*, No. e03602.

(60) Mu, F.; Zhou, X.; Fan, F.; Chen, Z.; Shi, G. A Fluorescence Biosensor for Therapeutic Drug Monitoring of Vancomycin Using In Vivo Microdialysis. *Anal. Chim. Acta* **2021**, *1151*, 338250.

(61) Jiang, S.; Wu, X.; Rommelfanger, N. J.; Ou, Z.; Hong, G. Shedding Light on Neurons: Optical Approaches for Neuromodulation. *Natl. Sci. Rev.* **2022**, *9*, nwac007.

(62) Cai, X.; Zhang, H.; Wei, P.; Liu, Q.; Sheng, D.; Li, Z.; Zhang, B.; Tang, G.; Zhao, W.; Ye, Z.; Xue, Z.; Xie, Y.; Dai, Y.; Wang, C.; Wang, Y.; Fu, X.; Yin, L.; Peng, H.; Ding, H.; Zhao, G. et al. A Wireless Optoelectronic Probe to Monitor Oxygenation in Deep Brain Tissue. *Nat. Photonics* **2024**, DOI: 10.1038/s41566-023-01374-y

(63) Sonmezoglu, S.; Fineman, J. R.; Maltepe, E.; Maharbiz, M. M. Monitoring Deep-Tissue Oxygenation with a Millimeter-Scale Ultrasonic Implant. *Nat. Biotechnol.* **2021**, *39*, 855−864.

(64) Lu, Y.; Driscoll, N.; Ozden, I.; Yu, Z.; Nurmikko, A. V. Modulating Dopamine Release by Optogenetics in Transgenic Mice Reveals Terminal Dopaminergic Dynamics. *Neurophotonics* **2015**, *2*, 031207.

(65) Xu, J.; Lee, H. Anti-Biofouling Strategies for Long-Term Continuous Use of Implantable Biosensors. *Chemosensors* **2020**, *8*, 66.

(66) Chan, D.; Chien, J.-C.; Axpe, E.; Blankemeier, L.; Baker, S. W.; Swaminathan, S.; Piunova, V. A.; Zubarev, D. Y.; Maikawa, C. L.; Grosskopf, A. K.; Mann, J. L.; Soh, H. T.; Appel, E. A. Combinatorial Polyacrylamide Hydrogels for Preventing Biofouling on Implantable Biosensors. *Adv. Mater.* **2022**, *34*, 2109764.

(67) Matthes, R. The International Commission on Non-Ionizing Radiation Protection. Guidelines on Limits of Exposure to Ultraviolet Radiation of Wavelengths between 180 and 400 nm (Incoherent Optical Radiation). *Health Phys.* **2004**, *87*, 171−186.

(68) Jeong, C.; Koirala, G. R.; Jung, Y. H.; Ye, Y. S.; Hyun, J. H.; Kim, T. H.; Park, B.; Ok, J.; Jung, Y.; Kim, T.-i. Motion Artifact-Resilient Zone for Implantable Sensors. *Adv. Funct. Mater.* **2022**, *32*, 2206461.

(69) Park, B.; Shin, J. H.; Ok, J.; Park, S.; Jung, W.; Jeong, C.; Choy, S.; Jo, Y. J.; Kim, T.-i. Cuticular Pad-Inspired Selective Frequency Damper for Nearly Dynamic Noise-Free Bioelectronics. *Science* **2022**, *376*, 624−629.